Chapter 7

Motivation. This chapter is devoted to "external" flows around bodies immersed in a fluid stream. Such a flow will have viscous (shear and no-slip) effects near the body surfaces and in its wake, but will typically be nearly inviscid far from the body. These are unconfined *boundary-layer* flows.

The technique of boundary-layer (BL) analysis can be used to compute viscous effects near solid walls and to "patch" these onto the outer inviscid motion. This patching is more successful as the body Reynolds number becomes larger, as shown in Fig. 7.1.

In Fig. 7.1 a uniform stream U moves parallel to a sharp flat plate of length L. If the Reynolds number UL/ν is low (Fig. 7.1a), the viscous region is very broad and extends far ahead and to the sides of the plate. The plate retards the oncoming stream greatly, and small changes in flow parameters cause large changes in the pressure distribution along the plate. Thus, although in principle it should be possible to patch the viscous and inviscid layers in a mathematical analysis, their interaction is strong and nonlinear [1 to 3]. There is no existing simple theory for external-flow analysis at Reynolds numbers from 1 to about 1000. Such thick-shear-layer flows are typically studied by experiment or by numerical modeling of the flow field on a digital computer [4].

A high-Reynolds-number flow (Fig. 7.1b) is much more amenable to boundary-layer patching, as first pointed out by Prandtl in 1904. The viscous layers, either laminar or turbulent, are very thin, thinner even than the drawing shows. We define the boundary-layer thickness δ as the locus of points where the velocity u parallel to the plate reaches 99 percent of the external velocity U.

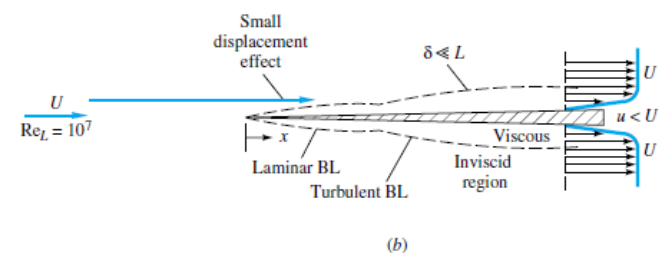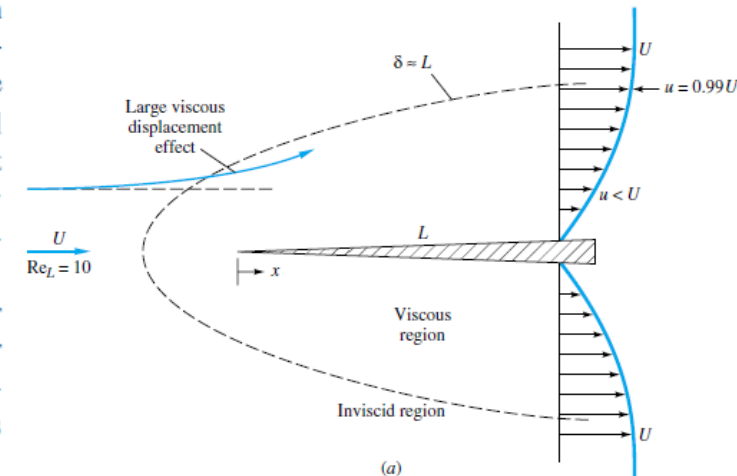| Re_x	10^4	10^5	10^6	10^7	10^8
$(\delta/x)_{lam}$	0.050	0.016	0.005		
$(\delta/x)_{turb}$			0.022	0.016	0.011

Fig. 7.1 Comparison of flow past a sharp flat plate at low and high Reynolds numbers: (*a*) laminar, low-Re flow; (*b*) high-Re flow.

Chapter 7 (Cont'd)

For slender bodies, such as plates and airfoils parallel to the oncoming stream, we conclude that this assumption of negligible interaction between the boundary layer and the outer pressure distribution is an excellent approximation.

For a blunt-body flow, however, even at very high Reynolds numbers, there is a discrepancy in the viscous-inviscid patching concept. Figure 7.2 shows two sketches of flow past a two- or three-dimensional blunt body. In the idealized sketch (7.2a), there is a thin film of boundary layer about the body and a narrow sheet of viscous wake in the rear. The patching theory would be glorious for this picture, but it is false.

The theory of strong interaction between blunt-body viscous and inviscid layers is not well developed. Flows like that of Fig. 7.2b are normally studied experimentally.
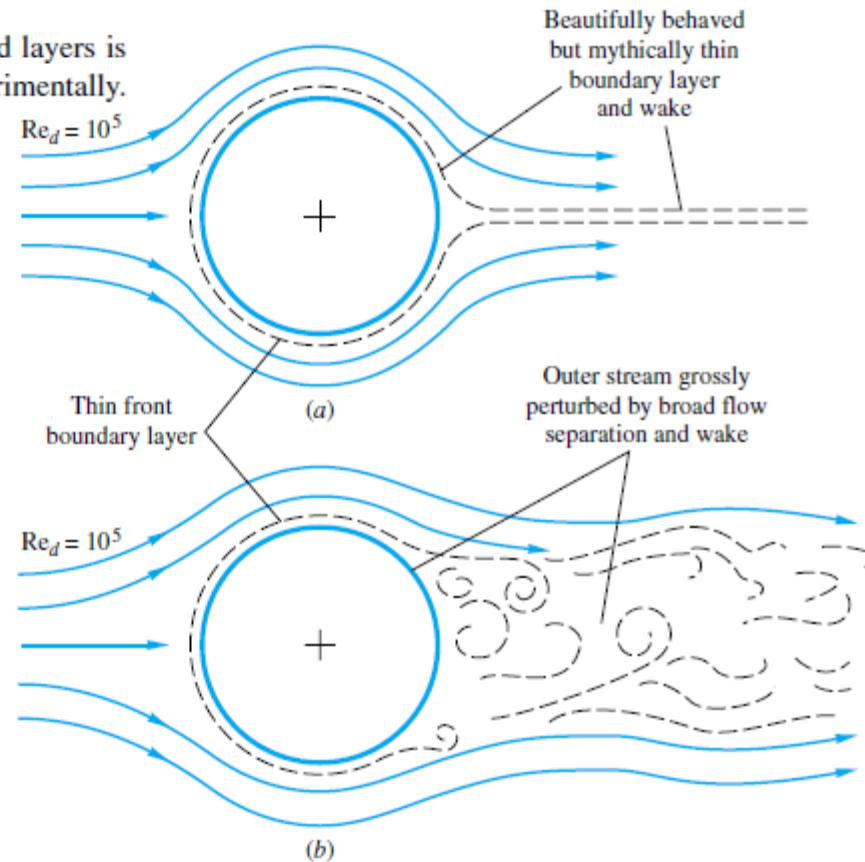

Fig. 7.2 Illustration of the strong interaction between viscous and inviscid regions in the rear of blunt-body flow: (a) idealized and definitely false picture of blunt-body flow; (b) actual picture of blunt-body flow.

Chapter 7 (Cont'd)

7.2 Momentum-Integral Estimates

CV analysis (laminar or turb.) gives:

$$D(x) = \rho b \int_0^{\delta(x)} u(U - u)\, dy \qquad (7.2)$$

Kármán's Analysis of the Flat Plate

Equation (7.2) was derived in 1921 by Kármán [7], who wrote it in the convenient form of the *momentum thickness* θ

$$D(x) = \rho b U^2 \theta \qquad \theta = \int_0^{\delta} \frac{u}{U}\left(1 - \frac{u}{U}\right) dy \qquad (7.3)$$

Momentum thickness is thus a measure of total plate drag. Kármán then noted that the drag also equals the integrated wall shear stress along the plate
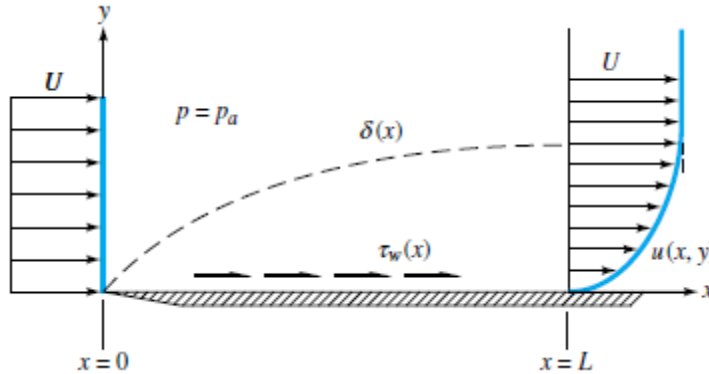
$$D(x) = b \int_0^x \tau_w(x)\, dx$$

or

$$\frac{dD}{dx} = b\tau_w \qquad (7.4)$$

Meanwhile, the derivative of Eq. (7.3), with $U = $ constant, is

$$\frac{dD}{dx} = \rho b U^2 \frac{d\theta}{dx}$$

By comparing this with Eq. (7.4) Kármán arrived at what is now called the *momentum-integral relation* for flat-plate boundary-layer flow

$$\tau_w = \rho U^2 \frac{d\theta}{dx} \qquad (7.5)$$

It is valid for either laminar or turbulent flat-plate flow.

Chapter 7 (Cont'd)

Displacement Thickness

Another interesting effect of a boundary layer is its small but finite displacement of the outer streamlines. As shown in Fig. 7.4, outer streamlines must deflect outward a distance $\delta^*(x)$ to satisfy conservation of mass between the inlet and outlet

$$\int_0^h \rho U b\, dy = \int_0^\delta \rho u b\, dy \qquad \delta = h + \delta^* \tag{7.11}$$

The quantity δ^* is called the *displacement thickness* of the boundary layer. To relate it to $u(y)$, cancel ρ and b from Eq. (7.11), evaluate the left integral, and slyly add and subtract U from the right integrand:

$$U h = \int_0^\delta (U + u - U)\, dy = U(h + \delta^*) + \int_0^\delta (u - U)\, dy$$

or

$$\delta^* = \int_0^\delta \left(1 - \frac{u}{U}\right) dy \tag{7.12}$$

Thus the ratio of δ^*/δ varies only with the dimensionless velocity-profile shape u/U.

Fig. 7.4 Displacement effect of a boundary layer.

Karman's laminar BL approximate solution:

To get a numerical result for laminar flow, Kármán assumed that the velocity profiles had an approximately parabolic shape

$$u(x, y) \approx U\left(\frac{2y}{\delta} - \frac{y^2}{\delta^2}\right) \qquad 0 \le y \le \delta(x) \tag{7.6}$$

Using the velocity profile he found the BL thickness, the shear-stress, and the momentum thickness as:

$$\frac{\delta}{x} \approx 5.5\left(\frac{\nu}{Ux}\right)^{1/2} = \frac{5.5}{Re_x^{1/2}} \qquad c_f = \frac{2\tau_w}{\rho U^2} \approx \left(\frac{8}{15}\right)^{1/2} = \frac{0.73}{Re_x^{1/2}} \qquad \approx \frac{1.83}{Re_x^{1/2}}$$

which are only 10% higher than the exact solution for laminar flat-plate flow (shown later). $\qquad \delta^* \approx \frac{1}{3}\delta$

The dimensionless quantity c_f, called the *skin-friction coefficient,* is analogous to the friction factor f in ducts.

Since δ^* is much smaller than x for large Re_x and the outer streamline slope V/U is proportional to δ^*, we conclude that the velocity normal to the wall is much smaller than the velocity parallel to the wall. This is a key assumption in boundary-layer theory
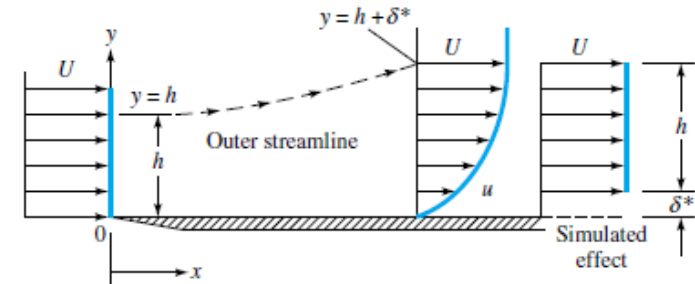
Chapter 7 (Cont'd)

7.3 The Boundary-Layer Equations

Derivation for Two-Dimensional Flow

the complete equations of motion consist of continuity and the x- and y-momentum relations

$$\frac{\partial u}{\partial x} + \frac{\partial v}{\partial y} = 0 \tag{7.14a}$$

$$\rho\left(u\frac{\partial u}{\partial x} + v\frac{\partial u}{\partial y}\right) = -\frac{\partial p}{\partial x} + \mu\left(\frac{\partial^2 u}{\partial x^2} + \frac{\partial^2 u}{\partial y^2}\right) \tag{7.14b}$$

$$\rho\left(u\frac{\partial v}{\partial x} + v\frac{\partial v}{\partial y}\right) = -\frac{\partial p}{\partial y} + \mu\left(\frac{\partial^2 v}{\partial x^2} + \frac{\partial^2 v}{\partial y^2}\right) \tag{7.14c}$$

In 1904 Prandtl correctly deduced that a shear layer must be very thin if the Reynolds number is large, so that the following approximations apply:

Velocities: $\qquad v \ll u$

Rates of change: $\qquad \dfrac{\partial u}{\partial x} \ll \dfrac{\partial u}{\partial y} \qquad \dfrac{\partial v}{\partial x} \ll \dfrac{\partial v}{\partial y} \qquad \dfrac{\partial^2 u}{\partial x^2} \ll \dfrac{\partial^2 u}{\partial y^2}$

Applying these approximations results in a powerful simplification

$$\frac{\partial p}{\partial y} \approx 0 \qquad \text{or} \qquad p \approx p(x) \text{ only}$$

In other words, the y-momentum equation can be neglected entirely, and the pressure varies only *along* the boundary layer, not through it. The pressure-gradient term $\frac{\partial p}{\partial x}$ is assumed to be known in advance from Bernoulli's equation applied to the outer inviscid flow

$$\frac{\partial p}{\partial x} = \frac{dp}{dx} = -\rho U\frac{dU}{dx}$$

Presumably we have already made the inviscid analysis and know the distribution of $U(x)$ along the wall (Chap. 8).

The net result is that the three full equations of motion (7.14) are reduced to Prandtl's two boundary-layer equations

Continuity: $$\frac{\partial u}{\partial x} + \frac{\partial v}{\partial y} = 0 \tag{7.19a}$$

Momentum along wall: $$u\frac{\partial u}{\partial x} + v\frac{\partial u}{\partial y} \approx U\frac{dU}{dx} + \frac{1}{\rho}\frac{\partial \tau}{\partial y} \tag{7.19b}$$

where $$\tau = \begin{cases} \mu\dfrac{\partial u}{\partial y} & \text{laminar flow} \\[3mm] \mu\dfrac{\partial u}{\partial y} - \rho\overline{u'v'} & \text{turbulent flow} \end{cases}$$

These are to be solved for $u(x, y)$ and $v(x, y)$, with $U(x)$ assumed to be a known function from the outer inviscid-flow analysis. There are two boundary conditions on u and one on v:

At $y = 0$ (wall): $u = v = 0$ (no slip)   (7.20a)

At $y = \delta(x)$ (outer stream): $u = U(x)$ (patching)   (7.20b)

Unlike the Navier-Stokes equations (7.14), which are mathematically elliptic and must be solved simultaneously over the entire flow field, the boundary-layer equations (7.19) are mathematically parabolic and are solved by beginning at the leading edge and marching downstream as far as you like, stopping at the separation point or earlier if you prefer.[2]

Chapter 7 (Cont'd)

7.4 The Flat-Plate Boundary Layer

Laminar Flow

For laminar flow past the plate, the boundary-layer equations (7.19) can be solved exactly for u and v, assuming that the free-stream velocity U is constant ($dU/dx = 0$). The solution was given by Prandtl's student Blasius, in his 1908 dissertation from Göttingen. With an ingenious coordinate transformation, Blasius showed that the dimensionless velocity profile u/U is a function only of the single composite dimensionless variable $(y)[U/(\nu x)]^{1/2}$:

$$\frac{u}{U} = f'(\eta) \qquad \eta = y\left(\frac{U}{\nu x}\right)^{1/2} \tag{7.21}$$

where the prime denotes differentiation with respect to η. Substitution of (7.21) into the boundary-layer equations (7.19) reduces the problem, after much algebra, to a single third-order nonlinear ordinary differential equation for f

$$f''' + \tfrac{1}{2}ff'' = 0 \tag{7.22}$$

The boundary conditions (7.20) become

At $y = 0$:
$$f(0) = f'(0) = 0 \tag{7.23a}$$

As $y \to \infty$:
$$f'(\infty) \to 1.0 \tag{7.23b}$$

This is the *Blasius equation*, for which accurate solutions have been obtained only by numerical integration. Some tabulated values of the velocity-profile shape $f'(\eta) = u/U$ are given in Table 7.1.

Since u/U approaches 1.0 only as $y \to \infty$, it is customary to select the boundary-layer thickness δ as that point where $u/U = 0.99$. From the table, this occurs at $\eta \approx 5.0$:

$$\delta_{99\%}\left(\frac{U}{\nu x}\right)^{1/2} \approx 5.0$$

or

$$\frac{\delta}{x} \approx \frac{5.0}{Re_x^{1/2}} \qquad \text{Blasius (1908)} \tag{7.24}$$

Table 7.1 The Blasius Velocity Profile [1 to 3]

$y[U/(\nu x)]^{1/2}$	u/U	$y[U/(\nu x)]^{1/2}$	u/U
0.0	0.0	2.8	0.81152
0.2	0.06641	3.0	0.84605
0.4	0.13277	3.2	0.87609
0.6	0.19894	3.4	0.90177
0.8	0.26471	3.6	0.92333
1.0	0.32979	3.8	0.94112
1.2	0.39378	4.0	0.95552
1.4	0.45627	4.2	0.96696
1.6	0.51676	4.4	0.97587
1.8	0.57477	4.6	0.98269
2.0	0.62977	4.8	0.98779
2.2	0.68132	5.0	0.99155
2.4	0.72899	∞	1.00000
2.6	0.77246		

With the profile known, Blasius, of course, could also compute the wall shear and displacement thickness

$$c_f = \frac{0.664}{Re_x^{1/2}} \qquad \frac{\delta^*}{x} = \frac{1.721}{Re_x^{1/2}} \qquad (7.25)$$

$$\tau_w(x) = \frac{0.332\rho^{1/2}\mu^{1/2}U^{1.5}}{x^{1/2}}$$

$$D(x) = b\int_0^x \tau_w(x)\,dx = 0.664b\rho^{1/2}\mu^{1/2}U^{1.5}x^{1/2}$$

$$C_D = \frac{2D(L)}{\rho U^2 bL} = \frac{1.328}{Re_L^{1/2}} = 2c_f(L)$$

This can be rewritten in terms of the momentum thickness at the trailing edge

$$C_D = \frac{2\theta(L)}{L}$$

Computation of θ from the profile u/U or from C_D gives

$$\frac{\theta}{x} = \frac{0.664}{Re_x^{1/2}} \qquad \text{laminar flat plate}$$

Since δ is so ill defined, the momentum thickness, being definite, is often used to correlate data taken for a variety of boundary layers under differing conditions. The ratio of displacement to momentum thickness, called the dimensionless-profile *shape factor*, is also useful in integral theories. For laminar flat-plate flow

$$H = \frac{\delta^*}{\theta} = \frac{1.721}{0.664} = 2.59 \qquad (7.31)$$

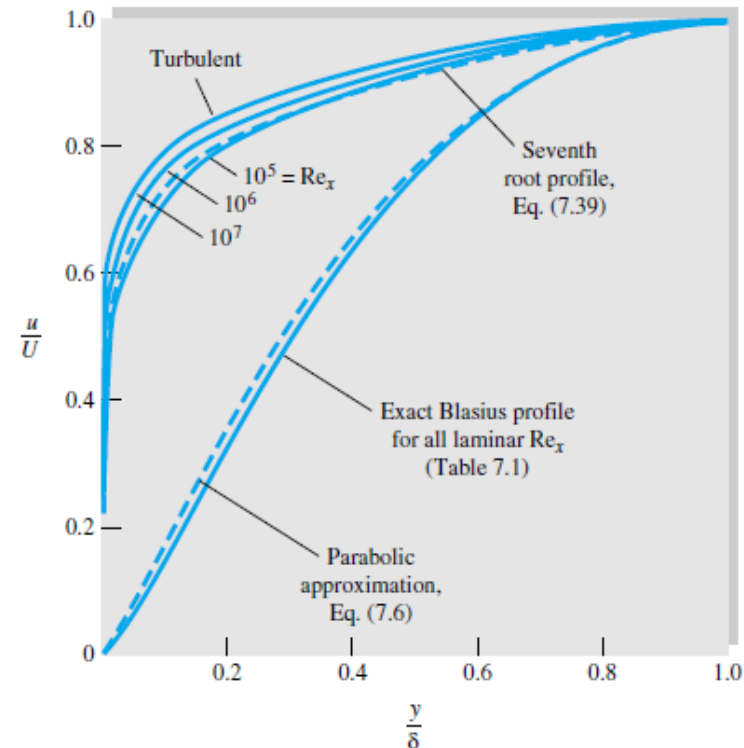A large shape factor then implies that boundary-layer separation is about to occur.

Fig. 7.5 Comparison of dimensionless laminar and turbulent flat-plate velocity profiles.

Chapter 7 (Cont'd)

Transition to Turbulence

The laminar flat-plate boundary layer eventually becomes turbulent, but there is no unique value for this change to occur. With care in polishing the wall and keeping the free stream quiet, one can delay the transition Reynolds number to $\mathrm{Re}_{x,tr} \approx 3$ E6 [8]. However, for typical commercial surfaces and gusty free streams, a more realistic value is $\mathrm{Re}_{x,tr} \approx 5$ E5.

Turbulent Flow

There is no exact theory for turbulent flat-plate flow, although there are many elegant computer solutions of the boundary-layer equations using various empirical models for the turbulent eddy viscosity [9]. The most widely accepted result is simply an integal analysis similar to our study of the laminar-profile approximation (7.6).

We begin with Eq. (7.5), which is valid for laminar or turbulent flow. We write it here for convenient reference:

$$\tau_w(x) = \rho U^2 \frac{d\theta}{dx} \tag{7.32}$$

From the definition of c_f, Eq. (7.10), this can be rewritten as

$$c_f = 2 \frac{d\theta}{dx} \tag{7.33}$$

Now recall from Fig. 7.5 that the turbulent profiles are nowhere near parabolic. Going back to Fig. 6.9, we see that flat-plate flow is very nearly logarithmic, with a slight outer wake and a thin viscous sublayer. Therefore, just as in turbulent pipe flow, we assume that the logarithmic law (6.21) holds all the way across the boundary layer

$$\frac{u}{u^*} \approx \frac{1}{\kappa} \ln \frac{yu^*}{\nu} + B \qquad u^* = \left(\frac{\tau_w}{\rho}\right)^{1/2} \tag{7.34}$$

with, as usual, $\kappa = 0.41$ and $B = 5.0$. At the outer edge of the boundary layer, $y = \delta$ and $u = U$, and Eq. (7.34) becomes

$$\frac{U}{u^*} = \frac{1}{\kappa} \ln \frac{\delta u^*}{\nu} + B \tag{7.35}$$

But the definition of the skin-friction coefficient, Eq. (7.10), is such that the following identities hold:

$$\frac{U}{u^*} \equiv \left(\frac{2}{c_f}\right)^{1/2} \qquad \frac{\delta u^*}{\nu} \equiv \mathrm{Re}_\delta \left(\frac{c_f}{2}\right)^{1/2} \tag{7.36}$$

Therefore Eq. (7.35) is a *skin-friction law* for turbulent flat-plate flow

$$\left(\frac{2}{c_f}\right)^{1/2} \approx 2.44 \ln \left[\mathrm{Re}_\delta \left(\frac{c_f}{2}\right)^{1/2}\right] + 5.0 \tag{7.37}$$

It is a complicated law, but we can at least solve for a few values and list them:

Re_δ	10^4	10^5	10^6	10^7
c_f	0.00493	0.00315	0.00217	0.00158

Following a suggestion of Prandtl, we can forget the complex log friction law (7.37) and simply fit the numbers in the table to a power-law approximation

$$c_f \approx 0.02 \, Re_\delta^{-1/6} \tag{7.38}$$

This we shall use as the left-hand side of Eq. (7.33). For the right-hand side, we need an estimate for $\theta(x)$ in terms of $\delta(x)$. If we use the logarithmic-law profile (7.34), we shall be up to our hips in logarithmic integrations for the momentum thickness. Instead we follow another suggestion of Prandtl, who pointed out that the turbulent profiles in Fig. 7.5 can be approximated by a one-seventh-power law

$$\left(\frac{u}{U}\right)_{turb} \approx \left(\frac{y}{\delta}\right)^{1/7} \tag{7.39}$$

With this simple approximation, the momentum thickness (7.28) can easily be evaluated:

$$\theta \approx \int_0^\delta \left(\frac{y}{\delta}\right)^{1/7} \left[1 - \left(\frac{y}{\delta}\right)^{1/7}\right] dy = \frac{7}{72}\delta \tag{7.40}$$

substitute into Kármán's momentum law and integrate, assuming $\delta = 0$ at $x = 0$:

$$Re_\delta \approx 0.16 \, Re_x^{6/7} \qquad or \qquad \frac{\delta}{x} \approx \frac{0.16}{Re_x^{1/7}} \tag{7.42}$$

$$c_f \approx \frac{0.027}{Re_x^{1/7}}$$

$$\tau_{w,turb} \approx \frac{0.0135\mu^{1/7}\rho^{6/7}U^{13/7}}{x^{1/7}}$$

$$C_D = \frac{0.031}{Re_L^{1/7}} = \frac{7}{6} c_f(L)$$

$$\delta^* \approx \int_0^\delta \left[1 - \left(\frac{y}{\delta}\right)^{1/7}\right] dy = \frac{1}{8}\delta$$

$$H = \frac{\delta^*}{\theta} = \frac{\frac{1}{8}}{\frac{7}{72}} = 1.3$$

Figure 7.6 shows flat-plate drag coefficients for both laminar-and turbulent-flow conditions. The smooth-wall relations (7.27) and (7.45) are shown, along with the effect of wall roughness, which is quite strong. The proper roughness parameter here is x/ϵ or L/ϵ, by analogy with the pipe parameter e/d. In the fully rough regime, C_D is independent of the Reynolds number, so that the drag varies exactly as U^2 and is independent of μ. Reference 2 presents a theory of rough flat-plate flow, and Ref. 1 gives a curve fit for skin friction and drag in the fully rough regime:

$$c_f \approx \left(2.87 + 1.58 \log \frac{x}{\epsilon}\right)^{-2.5} \qquad (7.48a)$$

$$C_D \approx \left(1.89 + 1.62 \log \frac{L}{\epsilon}\right)^{-2.5} \qquad (7.48b)$$

Equation (7.48b) is plotted to the right of the dashed line in Fig. 7.6. The figure also shows the behavior of the drag coefficient in the transition region $5 \times 10^5 < \text{Re}_L < 8 \times 10^7$, where the laminar drag at the leading edge is an appreciable fraction of the total drag. Schlichting [1] suggests the following curve fits for these transition drag curves depending upon the Reynolds number Re_{trans} where transition begins:

$$C_D \approx \begin{cases} \dfrac{0.031}{\text{Re}_L^{1/7}} - \dfrac{1440}{\text{Re}_L} & \text{Re}_{\text{trans}} = 5 \times 10^5 \qquad (7.49a) \\[4mm] \dfrac{0.031}{\text{Re}_L^{1/7}} - \dfrac{8700}{\text{Re}_L} & \text{Re}_{\text{trans}} = 3 \times 10^6 \qquad (7.49b) \end{cases}$$
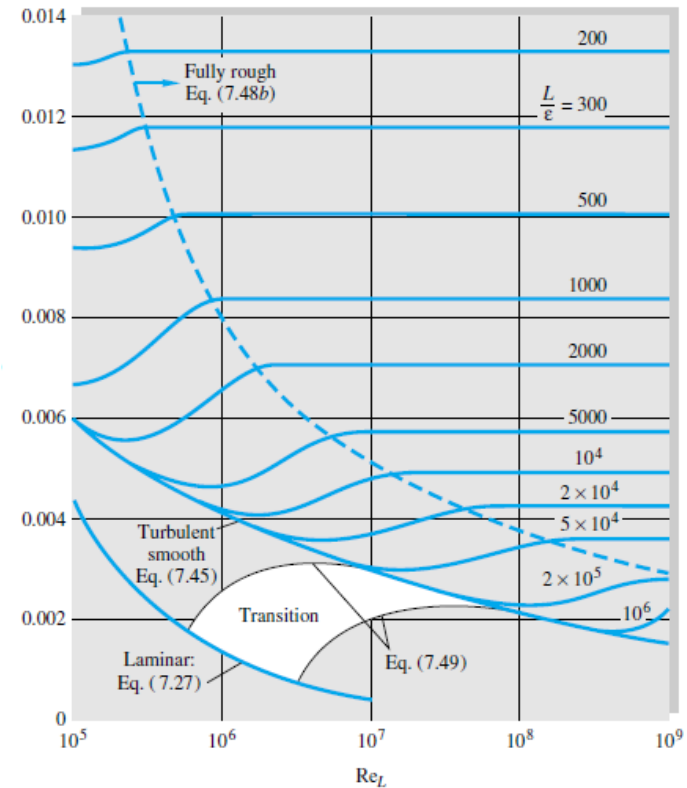

Fig. 7.6 Drag coefficient of laminar and turbulent boundary layers on smooth and rough flat plates. This chart is the flat-plate analog of the Moody diagram of Fig. 6.13.

7.5 Boundary Layers with Pressure Gradient[3]

The flat-plate analysis of the previous section should give us a good feeling for the behavior of both laminar and turbulent boundary layers, except for one important effect: flow separation. Prandtl showed that separation like that in Fig. 7.2b is caused by excessive momentum loss near the wall in a boundary layer trying to move downstream against increasing pressure, $dp/dx > 0$, which is called an *adverse pressure gradient*. The opposite case of decreasing pressure, $dp/dx < 0$, is called a *favorable gradient*, where flow separation can never occur. In a typical immersed-body flow, e.g., Fig. 7.2b, the favorable gradient is on the front of the body and the adverse gradient is in the rear, as discussed in detail in Chap. 8.

We can explain flow separation with a geometric argument about the second derivative of velocity u at the wall. From the momentum equation (7.19b) at the wall, where $u = v = 0$, we obtain

$$\left.\frac{\partial \tau}{\partial y}\right|_{wall} = \mu \left.\frac{\partial^2 u}{\partial y^2}\right|_{wall} = -\rho U \frac{dU}{dx} = \frac{dp}{dx}$$

or

$$\left.\frac{\partial^2 u}{\partial y^2}\right|_{wall} = \frac{1}{\mu}\frac{dp}{dx} \qquad (7.50)$$

for either laminar or turbulent flow. Thus in an adverse gradient the second derivative of velocity is positive at the wall; yet it must be negative at the outer layer ($y = \delta$) to merge smoothly with the mainstream flow $U(x)$. It follows that the second derivative must pass through zero somewhere in between, at a point of inflection, and any boundary-layer profile in an adverse gradient must exhibit a characteristic S shape.

Figure 7.7 illustrates the general case. In a favorable gradient (Fig. 7.7a) the profile is very rounded, there is no point of inflection, there can be no separation, and laminar profiles of this type are very resistant to a transition to turbulence [1 to 3].

In a zero pressure gradient (Fig. 7.7b), e.g., flat-plate flow, the point of inflection is at the wall itself. There can be no separation, and the flow will undergo transition at Re_x no greater than about 3×10^6, as discussed earlier.

In an adverse gradient (Fig. 7.7c to e), a point of inflection (PI) occurs in the boundary layer, its distance from the wall increasing with the strength of the adverse gradient. For a weak gradient (Fig. 7.7c) the flow does not actually separate, but it is vulnerable to transition to turbulence at Re_x as low as 10^5 [1, 2]. At a moderate gradient, a critical condition (Fig. 7.7d) is reached where the wall shear is exactly zero ($\partial u/\partial y = 0$). This is defined as the *separation point* ($\tau_w = 0$), because any stronger gradient will actually cause backflow at the wall (Fig. 7.7e): the boundary layer thickens greatly, and the main flow breaks away, or separates, from the wall (Fig. 7.2b).
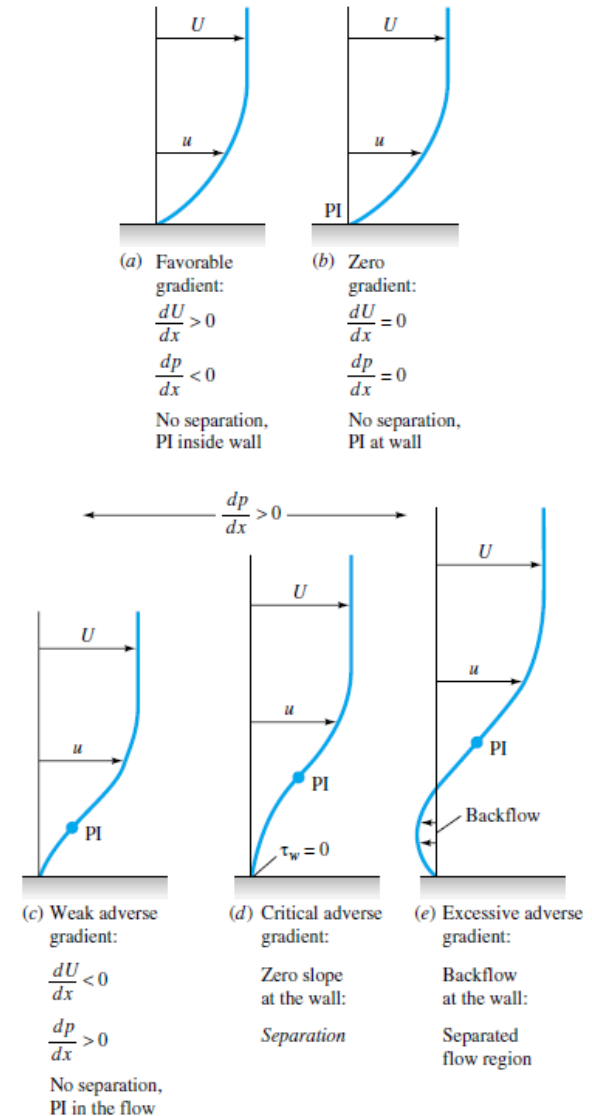

(a) Favorable gradient:
$$\frac{dU}{dx} > 0$$
$$\frac{dp}{dx} < 0$$
No separation, PI inside wall

(b) Zero gradient:
$$\frac{dU}{dx} = 0$$
$$\frac{dp}{dx} = 0$$
No separation, PI at wall

$$\frac{dp}{dx} > 0$$

(c) Weak adverse gradient:
$$\frac{dU}{dx} < 0$$
$$\frac{dp}{dx} > 0$$
No separation, PI in the flow

(d) Critical adverse gradient:
Zero slope at the wall:
Separation

(e) Excessive adverse gradient:
Backflow at the wall:
Separated flow region

Fig. 7.7 Effect of pressure gradient on boundary-layer profiles; PI = point of inflection.

Chapter 7 (Cont'd)

Laminar Integral Theory

extend to variable $U(x)$

$$\frac{\tau_w}{\rho U^2} = \frac{1}{2} c_f = \frac{d\theta}{dx} + (2 + H) \frac{\theta}{U} \frac{dU}{dx} \qquad (7.51)$$

where $\theta(x)$ is the momentum thickness and $H(x) = \delta^*(x)/\theta(x)$ is the shape factor. negative dU/dx is equivalent to positive dp/dx, that is, an adverse gradient.

We can integrate Eq. (7.51) to determine $\theta(x)$ for a given $U(x)$ if we correlate c_f and H with the momentum thickness. This has been done by examining typical velocity profiles of laminar and turbulent boundary-layer flows for various pressure gradients. Some examples are given in Fig. 7.9, showing that the shape factor H is a good indicator of the pressure gradient. The higher the H, the stronger the adverse gradient, and separation occurs approximately at

$$H \approx \begin{cases} 3.5 & \text{laminar flow} \\ 2.4 & \text{turbulent flow} \end{cases} \qquad (7.52)$$

The laminar profiles (Fig. 7.9a) clearly exhibit the S shape and a point of inflection with an adverse gradient. But in the turbulent profiles (Fig. 7.9b) the points of inflection are typically buried deep within the thin viscous sublayer, which can hardly be seen on the scale of the figure.
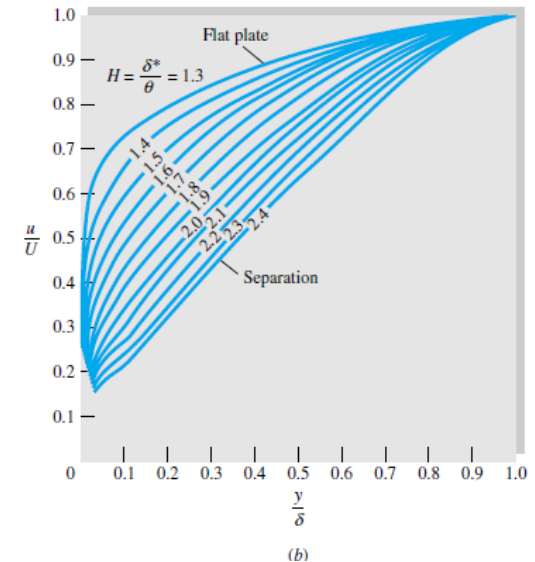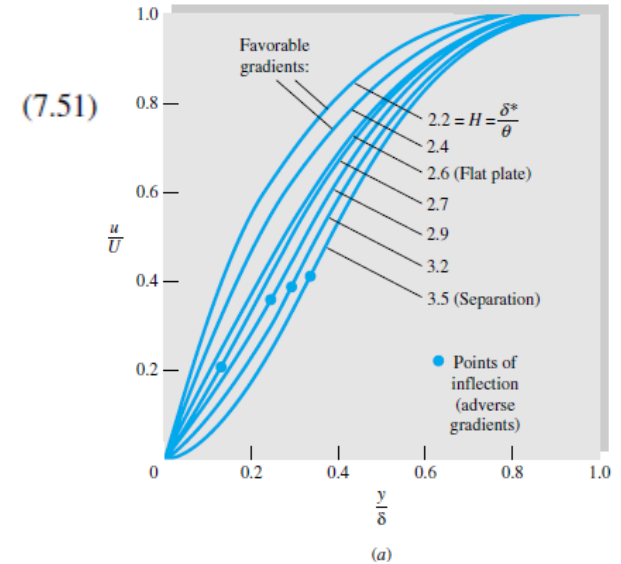
Fig. 7.9 Velocity profiles with pressure gradient: (a) laminar flow; (b) turbulent flow with adverse gradients.

Chapter 7 (Cont'd)

For laminar flow, a simple and effective method was developed by Thwaites [11], who found that Eq. (7.51) can be correlated by a single dimensionless momentum-thickness variable λ, defined as

$$\lambda = \frac{\theta^2}{\nu}\frac{dU}{dx} \tag{7.53}$$

Using a straight-line fit to his correlation, Thwaites was able to integrate Eq. (7.51) in closed form, with the result

$$\theta^2 = \theta_0^2\left(\frac{U_0}{U}\right)^6 + \frac{0.45\nu}{U^6}\int_0^x U^5\,dx \tag{7.54}$$

where θ_0 is the momentum thickness at $x = 0$ (usually taken to be zero). Separation ($c_f = 0$) was found to occur at a particular value of λ

Separation: $\qquad\qquad\qquad \lambda = -0.09 \qquad\qquad\qquad\qquad$ (7.55)

Finally, Thwaites correlated values of the dimensionless shear stress $S = \tau_w\theta/(\mu U)$ with λ, and his graphed result can be curve-fitted as follows:

$$S(\lambda) = \frac{\tau_w\theta}{\mu U} \approx (\lambda + 0.09)^{0.62} \tag{7.56}$$

This parameter is related to the skin friction by the identity

$$S \equiv \tfrac{1}{2}c_f\,\mathrm{Re}_\theta \tag{7.57}$$

As a demonstration of Thwaites' method, take a flat plate, where U = constant, $\lambda = 0$, and $\theta_0 = 0$. Equation (7.54) integrates to

$$\theta^2 = \frac{0.45\nu x}{U}$$

or $\qquad\qquad\qquad \dfrac{\theta}{x} = \dfrac{0.671}{\mathrm{Re}_x^{1/2}} \qquad\qquad\qquad\qquad$ (7.58)

This is within 1 percent of Blasius' exact solution, Eq. (7.30).

7.6 Experimental External Flows

Drag of Immersed Bodies

In low-speed flow past geometrically similar bodies with identical orientation and relative roughness, the drag coefficient should be a function of the body Reynolds number

$$C_D = f(\text{Re}) \tag{7.60}$$

The Reynolds number is based upon the free-stream velocity V and a characteristic length L of the body, usually the chord or body length parallel to the stream

$$\text{Re} = \frac{VL}{\nu} \tag{7.61}$$

For cylinders, spheres, and disks, the characteristic length is the diameter D.

Characteristic Area

Drag coefficients are defined by using a characteristic area A which may differ depending upon the body shape:

$$C_D = \frac{\text{drag}}{\frac{1}{2}\rho V^2 A} \tag{7.62}$$

The factor $\frac{1}{2}$ is our traditional tribute to Euler and Bernoulli. The area A is usually one of three types:

1. *Frontal area,* the body as seen from the stream; suitable for thick, stubby bodies, such as spheres, cylinders, cars, missiles, projectiles, and torpedoes.
2. *Planform area,* the body area as seen from above; suitable for wide, flat bodies such as wings and hydrofoils.
3. *Wetted area,* customary for surface ships and barges.

In using drag or other fluid-force data, it is important to note what length and area are being used to scale the measured coefficients.

Friction Drag and Pressure Drag

$$C_D = C_{D,press} + C_{D,fric}$$

The relative contribution of friction and pressure drag depends upon the body's shape, especially its thickness. Figure 7.12 shows drag data for a streamlined cylinder of very large depth into the paper. At zero thickness the body is a flat plate and exhibits 100 percent friction drag. At thickness equal to the chord length, simulating a circular cylinder, the friction drag is only about 3 percent. Friction and pressure drag are about equal at thickness $t/c = 0.25$. Note that C_D in Fig. 7.12b looks quite different when based upon frontal area instead of planform area, planform being the usual choice for this body shape. The two curves in Fig. 7.12b represent exactly the same drag data.
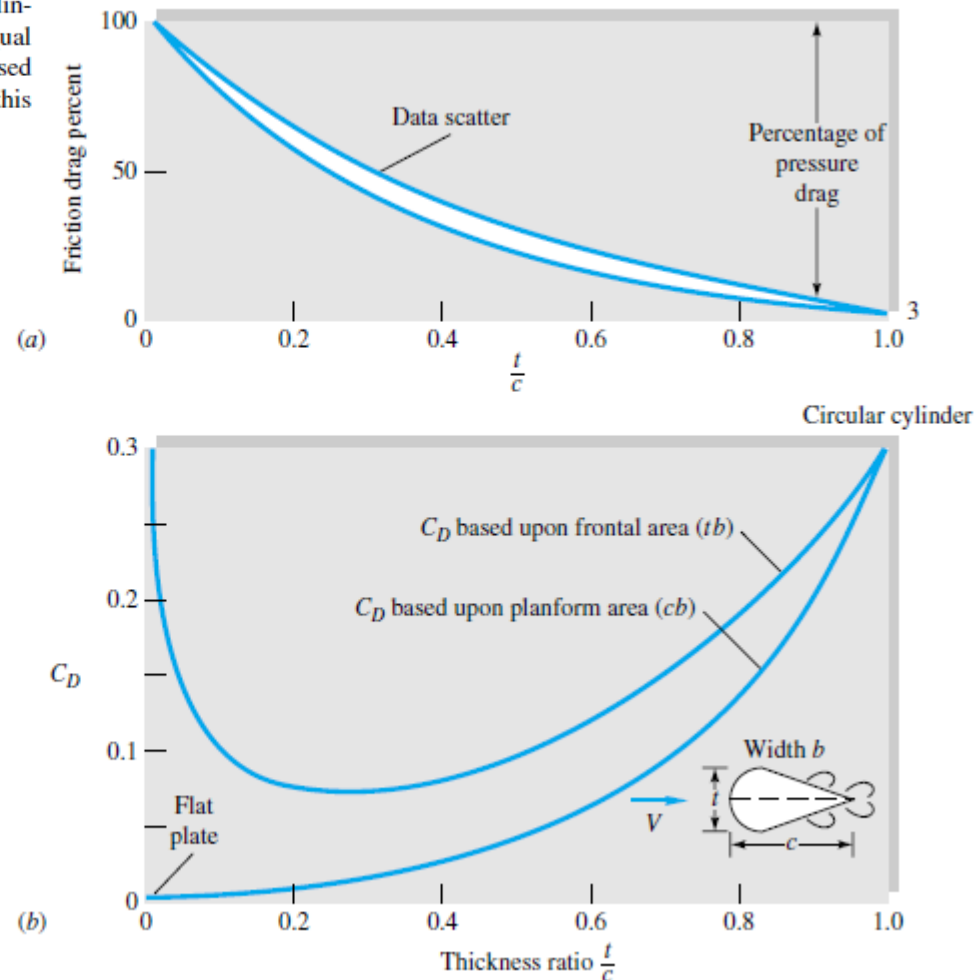
Fig. 7.12 Drag of a streamlined two-dimensional cylinder at $Re_c = 10^6$: (a) effect of thickness ratio on percentage of friction drag; (b) total drag versus thickness when based upon two different areas.

Chapter 7 (Cont'd)

Figure 7.13 illustrates the dramatic effect of separated flow

(a) $C_D = 1.2$ 82°   Separation   Broad wake

(b) $C_D = 0.3$ 120°   Separation   Narrow wake

(c)
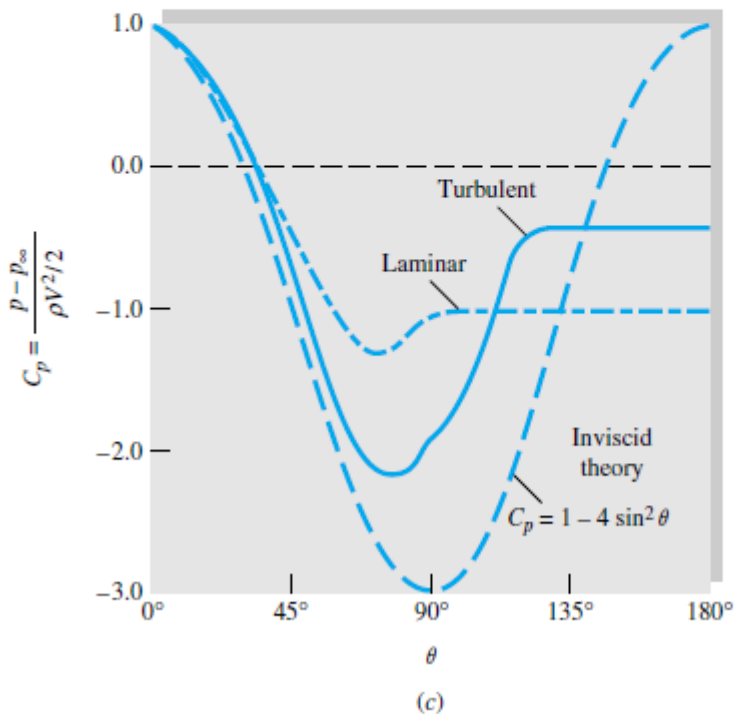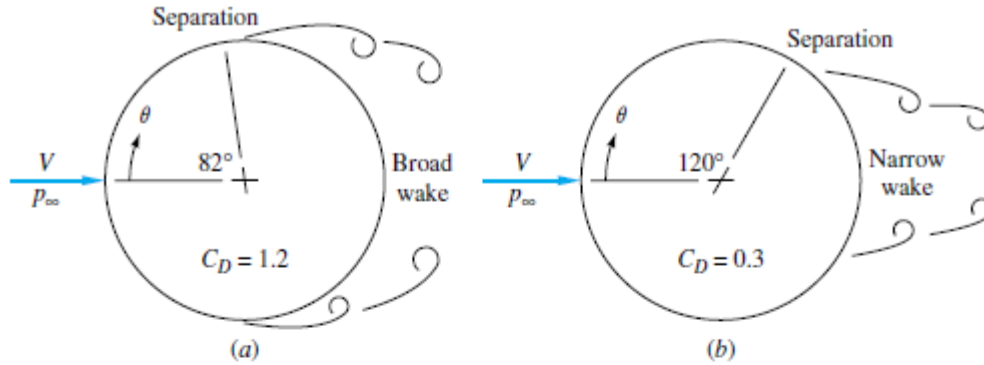
Fig. 7.13 Flow past a circular cylinder: (a) laminar separation; (b) turbulent separation; (c) theoretical and actual surface-pressure distributions.
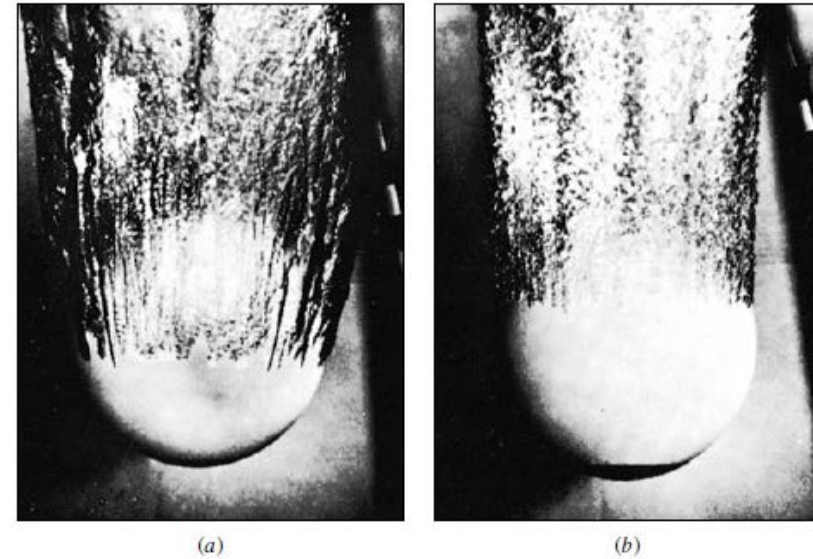
Fig. 7.14 Strong differences in laminar and turbulent separation on an 8.5-in bowling ball entering water at 25 ft/s: (a) smooth ball, laminar boundary layer; (b) same entry, turbulent flow induced by patch of nose-sand roughness. (*U.S. Navy photograph, Ordnance Test Station, Pasadena Annex.*)

The laminar flow (Fig. 7.14a) separates at about 80°, $C_D = 0.5$, while the turbulent flow (Fig. 7.14b) separates at 120°, $C_D = 0.2$.

Chapter 7 (Cont'd)

In general, we cannot overstress the importance of body streamlining to reduce drag at Reynolds numbers above about 100. This is illustrated in Fig. 7.15. The rectangular cylinder (Fig. 7.15a) has rampant separation at all sharp corners and very high drag. Rounding its nose (Fig. 7.15b) reduces drag by about 45 percent, but C_D is still high. Streamlining its rear to a sharp trailing edge (Fig. 7.15c) reduces its drag another 85 percent to a practical minimum for the given thickness. As a dramatic contrast, the circular cylinder (Fig. 7.15d) has one-eighth the thickness and one-three-hundredth the cross section (c) (Fig. 7.15c), yet it has the same drag. For high-performance vehicles and other moving bodies, the name of the game is drag reduction, for which intense research continues for both aerodynamic and hydrodynamic applications [20, 39].
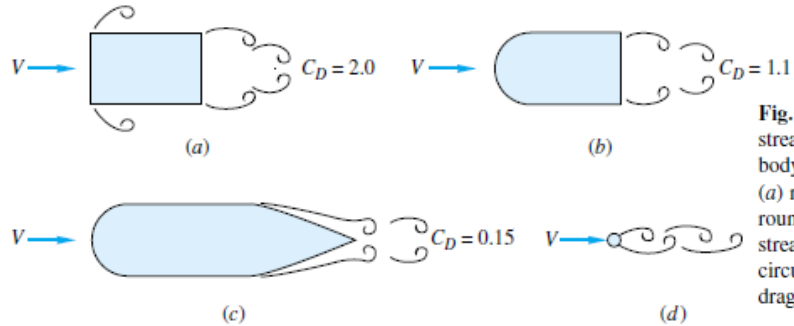
Fig. 7.15 The importance of streamlining in reducing drag of a body (C_D based on frontal area): (a) rectangular cylinder; (b) rounded nose; (c) rounded nose and streamlined sharp trailing edge; (d) circular cylinder with the same drag as case (c).

The drag of some representative wide-span (nearly two-dimensional) bodies is shown versus the Reynolds number in Fig. 7.16a. All bodies have high C_D at very low (*creeping flow*) Re ≤ 1.0, while they spread apart at high Reynolds numbers according to their degree of streamlining. All values of C_D are based on the planform area except the plate normal to the flow. The birds and the sailplane are, of course, not very two-dimensional, having only modest span length. Note that birds are not nearly as efficient as modern sailplanes or airfoils [14, 15].
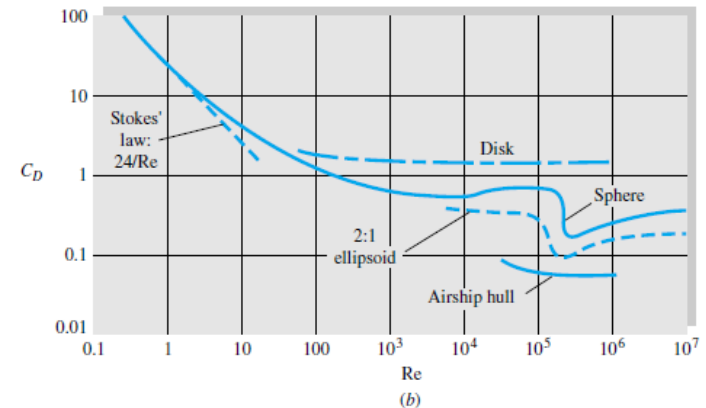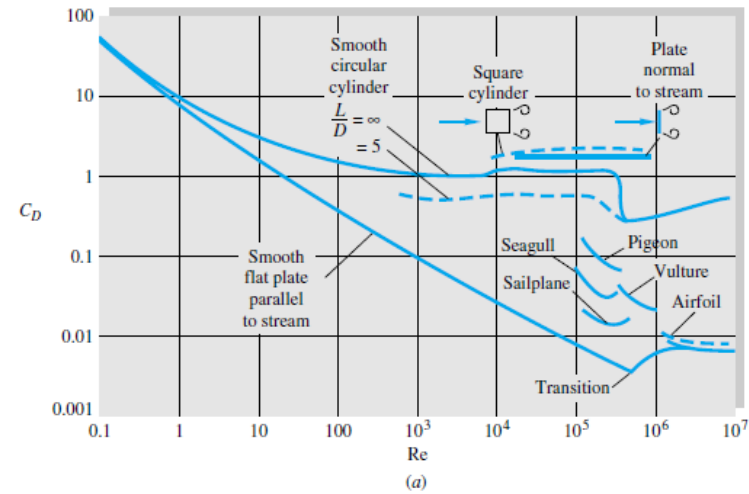

Fig. 7.16 Drag coefficients of smooth bodies at low Mach numbers: (a) two-dimensional bodies; (b) three-dimensional bodies. Note the Reynolds-number independence of blunt bodies at high Re.

Chapter 7 (Cont'd)

Table 7.2 gives a few data on drag, based on frontal area, of two-dimensional bodies of various cross section, at Re ≥ 10^4. The sharp-edged bodies, which tend to cause flow separation regardless of the character of the boundary layer, are insensitive to the Reynolds number. The elliptic cylinders, being smoothly rounded, have the laminar-to-turbulent transition effect of Figs. 7.13 and 7.14 and are therefore quite sensitive to whether the boundary layer is laminar or turbulent.

Shape	C_D based on frontal area	Shape	C_D based on frontal area	Shape	C_D based on frontal area
Square cylinder:	2.1	Half-cylinder:	1.2	Plate:	2.0
	1.6		1.7	Thin plate normal to a wall:	1.4
Half tube:	1.2	Equilateral triangle:	1.6		
	2.3		2.0	Hexagon:	1.0 | 0.7

Shape	C_D based on frontal area				
Rounded nose section:					
	L/H:	0.5	1.0	2.0	4.0	6.0
	C_D:	1.16	0.90	0.70	0.68	0.64

Flat nose section								
	L/H:	0.1	0.4	0.7	1.2	2.0	2.5	3.0	6.0
	C_D:	1.9	2.3	2.7	2.1	1.8	1.4	1.3	0.9

Elliptical cylinder:	Laminar	Turbulent
1:1	1.2	0.3
2:1	0.6	0.2
4:1	0.35	0.15
8:1	0.25	0.1

Table 7.2 Drag of Two-Dimensional Bodies at Re ≥ 10^4

Some drag coefficients of three-dimensional bodies are listed in Table 7.3 and Fig. 7.16b. Again we can conclude that sharp edges always cause flow separation and high drag which is insensitive to the Reynolds number. Rounded bodies like the ellipsoid have drag which depends upon the point of separation, so that both the Reynolds number and the character of the boundary layer are important. Body length will generally decrease pressure drag by making the body relatively more slender, but sooner or later the friction drag will catch up. For the flat-faced cylinder in Table 7.3, pressure drag decreases with L/d but friction increases, so that minimum drag occurs at about $L/d = 2$.

Table 7.3 Drag of Three-Dimensional Bodies at Re $\geq 10^4$

Body	C_D based on frontal area
Cube:	1.07
	0.81
Cup:	1.4
	0.4
Disk:	1.17
Parachute (Low porosity):	1.2

Cone:

θ:	10°	20°	30°	40°	60°	75°	90°
C_D:	0.30	0.40	0.55	0.65	0.80	1.05	1.15

Short cylinder, laminar flow:

L/D:	1	2	3	5	10	20	40	∞
C_D:	0.64	0.68	0.72	0.74	0.82	0.91	0.98	1.20

Porous parabolic dish [23]:

Porosity:	0	0.1	0.2	0.3	0.4	0.5
C_D:	1.42	1.33	1.20	1.05	0.95	0.82
C_D:	0.95	0.92	0.90	0.86	0.83	0.80

Average person: $C_D A \approx 9$ ft^2 $C_D A \approx 1.2$ ft^2

Pine and spruce trees [24]:

U, m/s:	10	20	30	40
C_D:	1.2 ± 0.2	1.0 ± 0.2	0.7 ± 0.2	0.5 ± 0.2

Body	Ratio	C_D based on frontal area
Rectangular plate:	b/h 1	1.18
	5	1.2
	10	1.3
	20	1.5
	∞	2.0

Body		Ratio		C_D based on frontal area	
Ellipsoid:				Laminar	Turbulent
		L/d 0.75		0.5	0.2
		1		0.47	0.2
		2		0.27	0.13
		4		0.25	0.1
		8		0.2	0.08

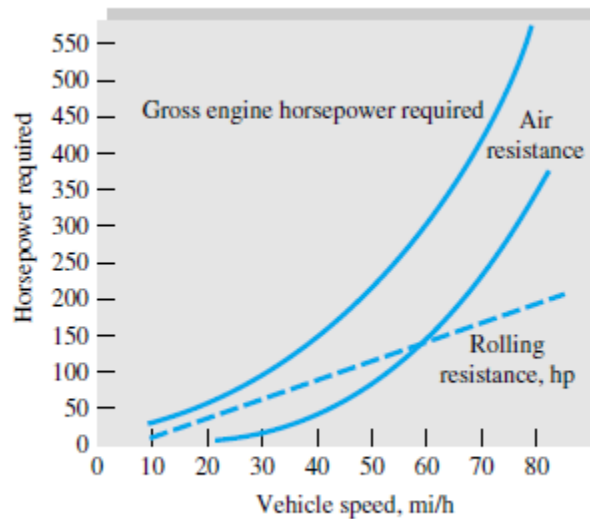| Body	Ratio	C_D based on frontal area
Flat-faced cylinder:	L/d 0.5	1.15
	1	0.90
	2	0.85
	4	0.87
	8	0.99

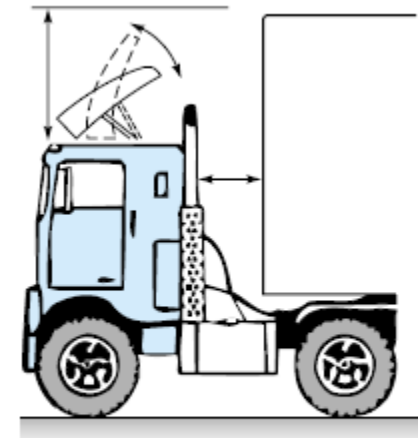# Chapter 7 (Cont'd)

Aerodynamic Forces on Road Vehicles

Fig. 7.17 Aerodynamics of automobiles: (*a*) the historical trend for drag coefficients [From Ref. 21]:
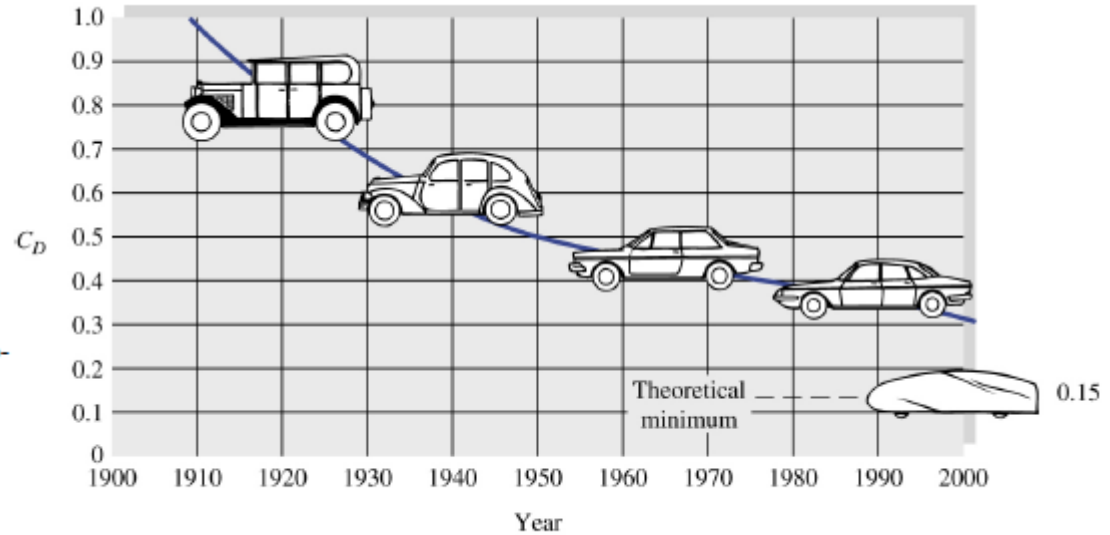
Fig. 7.18 Drag reduction of a tractor-trailer truck: (*a*) horsepower required to overcome resistance; (*b*) deflector added to cab reduces air drag by 20 percent. (*Uniroyal Inc.*)

Drag of Surface Ships

The drag data above, such as Tables 7.2 and 7.3, are for bodies "fully immersed" in a free stream, i.e., with no free surface. If, however, the body moves at or near a free liquid surface, *wave-making drag* becomes important and is dependent upon both the Reynolds number and the Froude number. To move through a water surface, a ship must create waves on both sides. This implies putting energy into the water surface and requires a finite drag force to keep the ship moving, even in a frictionless fluid. The total drag of a ship can then be approximated as the sum of friction drag and wave-making drag:

$$F \approx F_{\text{fric}} + F_{\text{wave}} \qquad \text{or} \qquad C_D \approx C_{D,\text{fric}} + C_{D,\text{wave}}$$

The friction drag can be estimated by the (turbulent) flat-plate formula, Eq. (7.45), based on the below-water or *wetted area* of the ship.

Reference 27 is an interesting review of both theory and experiment for wake-making surface ship drag. Generally speaking, the bow of the ship creates a wave system whose wavelength is related to the ship speed but not necessarily to the ship length. If the stern of the ship is a wave *trough*, the ship is essentially climbing uphill and has high wave drag. If the stern is a wave crest, the ship is nearly level and has lower drag. The criterion for these two conditions results in certain approximate Froude numbers [27]:

$$\text{Fr} = \frac{V}{\sqrt{gL}} \approx \frac{0.53}{\sqrt{N}} \qquad \begin{array}{l} \text{high drag if } N = 1, 3, 5, 7, \ldots ; \\ \text{low drag if } N = 2, 4, 6, 8, \ldots \end{array} \qquad (7.65)$$

where V is the ship's speed, L is the ship's length along the centerline, and N is the number of half-lengths, from bow to stern, of the drag-making wave system. The wave drag will increase with the Froude number and oscillate between lower drag (Fr ≈ 0.38, 0.27, 0.22, . . .) and higher drag (Fr ≈ 0.53, 0.31, 0.24, . . .) with negligible variation for Fr < 0.2. Thus it is best to design a ship to cruise at $N = 2, 4, 6, 8$. Shaping the bow and stern can further reduce wave-making drag.

Figure 7.19 shows the data of Inui [27] for a model ship. The main hull, curve A, shows peaks and valleys in wave drag at the appropriate Froude numbers > 0.2. Introduction of a *bulb* protrusion on the bow, curve B, greatly reduces the drag. Adding a second bulb to the stern, curve C, is still better, and Inui recommends that the design speed of this two-bulb ship be at $N = 4$, Fr ≈ 0.27, which is a nearly "waveless" condition. In this figure $C_{D,\text{wave}}$ is defined as $2F_{\text{wave}}/(\rho V^2 L^2)$ instead of using the wetted area.

The solid curves in Fig. 7.19 are based on potential-flow theory for the below-water hull shape. Chapter 8 is an introduction to potential-flow theory. Modern digital computers can be programmed for numerical CFD solutions of potential flow over the hulls of ships, submarines, yachts, and sailboats, including boundary-layer effects driven by the potential flow [28]. Thus theoretical prediction of flow past surface ships is now at a fairly high level. See also Ref. 15.
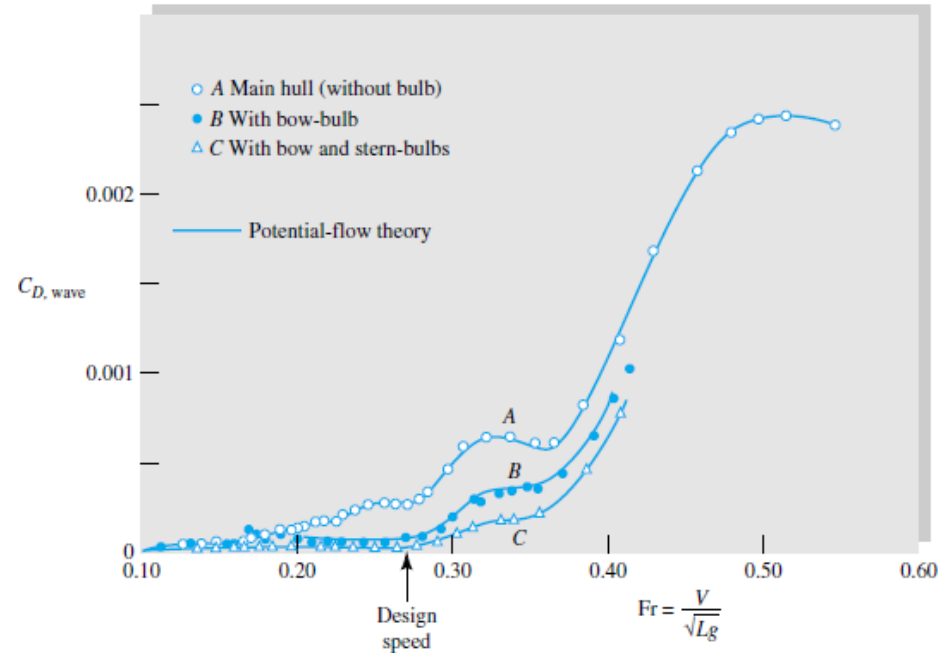

Fig. 7.19 Wave-making drag on a ship model. (*After Inui* [27].) *Note:* The drag coefficient is defined as $C_{DW} = 2F/(\rho V^2 L^2)$.

Body Drag at High Mach Numbers

All the data presented above are for nearly incompressible flows, with Mach numbers assumed less than about 0.5. Beyond this value compressibility can be very important, with $C_D = fcn(Re, Ma)$. As the stream Mach number increases, at some subsonic value $Ma_{crit} < 1$ which depends upon the body's bluntness and thickness, the local velocity at some point near the body surface will become sonic. If Ma increases beyond Ma_{crit}, shock waves form, intensify, and spread, raising surface pressures near the front of the body and therefore increasing the pressure drag. The effect can be dramatic with C_D increasing tenfold, and 70 years ago this sharp increase was called the *sonic barrier*, implying that it could not be surmounted. Of course, it can be—the rise in C_D is finite, as supersonic bullets have proved for centuries.

Figure 7.20 shows the effect of the Mach number on the drag coefficient of various body shapes tested in air.[5] We see that compressibility affects blunt bodies earlier, with Ma_{crit} equal to 0.4 for cylinders, 0.6 for spheres, and 0.7 for airfoils and pointed projectiles. Also the Reynolds number (laminar versus turbulent boundary-layer flow) has a large effect below Ma_{crit} for spheres and cylinders but becomes unimportant above $Ma \approx 1$. In contrast, the effect of the Reynolds number is small for airfoils and projectiles and is not shown in Fig. 7.20. A general statement might divide Reynolds- and Mach-number effects as follows:

$Ma \leq 0.4$:	Reynolds number important, Mach number unimportant
$0.4 < Ma < 1$:	both Reynolds and Mach numbers important
$Ma > 1.0$:	Reynolds number unimportant, Mach number important

At supersonic speeds, a broad *bow shock wave* forms in front of the body (see Figs. 9.10b and 9.19), and the drag is mainly due to high shock-induced pressures on the front. Making the bow a sharp point can sharply reduce the drag (Fig. 9.28) but does not eliminate the bow shock. Chapter 9 gives a brief treatment of compressibility. References 30 and 31 are more advanced textbooks devoted entirely to compressible flow.
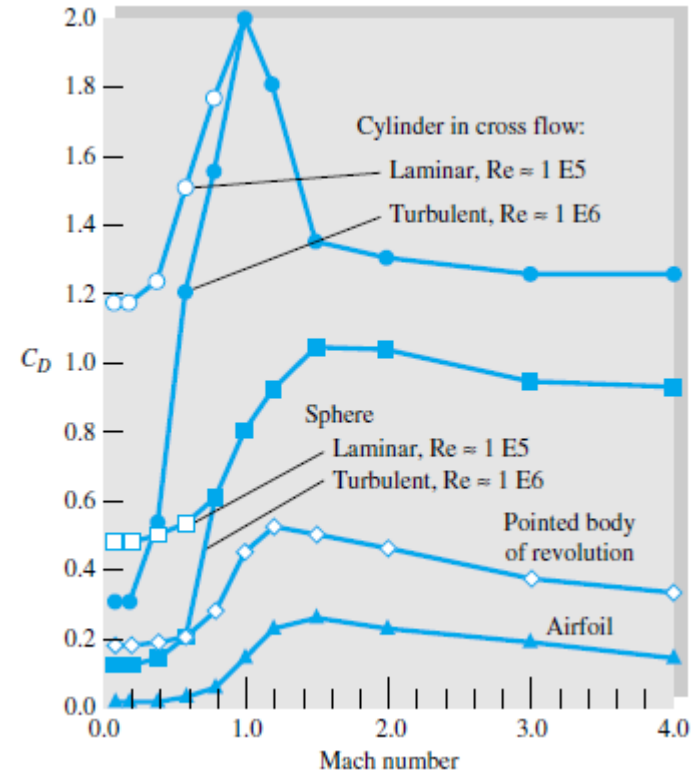

Fig. 7.20 Effect of the Mach number on the drag of various body shapes. (*Data from Refs. 23 and 29.*)

Forces on Lifting Bodies

Lifting bodies (airfoils, hydrofoils, or vanes) are intended to provide a large force normal to the free stream and as little drag as possible. Conventional design practice has evolved a shape not unlike a bird's wing, i.e., relatively thin ($t/c \leq 0/18$) with a rounded leading edge and a sharp trailing edge. A typical shape is sketched in Fig. 7.22.

For our purposes we consider the body to be symmetric, as in Fig. 7.11, with the free-stream velocity in the vertical plane. If the chord line between the leading and trailing edge is not a line of symmetry, the airfoil is said to be *cambered*. The camber line is the line midway between the upper and lower surfaces of the vane.

The angle between the free stream and the chord line is called the *angle of attack* α. The lift L and the drag D vary with this angle. The dimensionless forces are defined with respect to the planform area $A_p = bc$:

Lift coefficient:
$$C_L = \frac{L}{\frac{1}{2}\rho V^2 A_p} \qquad (7.66a)$$

Drag coefficient:
$$C_D = \frac{D}{\frac{1}{2}\rho V^2 A_p} \qquad (7.66b)$$

For low-speed flow with a given roughness ratio, C_L and C_D should vary with α and the chord Reynolds number

$$C_L = f(\alpha, \text{Re}_c) \qquad \text{or} \qquad C_D = f(\alpha, \text{Re}_c)$$

where $\text{Re}_c = Vc/\nu$. The Reynolds numbers are commonly in the turbulent-boundary-layer range and have a modest effect.

The rounded leading edge prevents flow separation there, but the sharp trailing edge causes a separation which generates the lift. Figure 7.23 shows what happens when a flow starts up past a lifting vane or an airfoil.
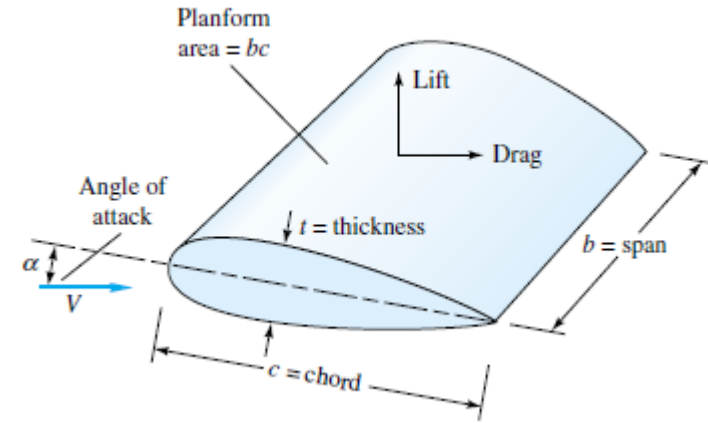

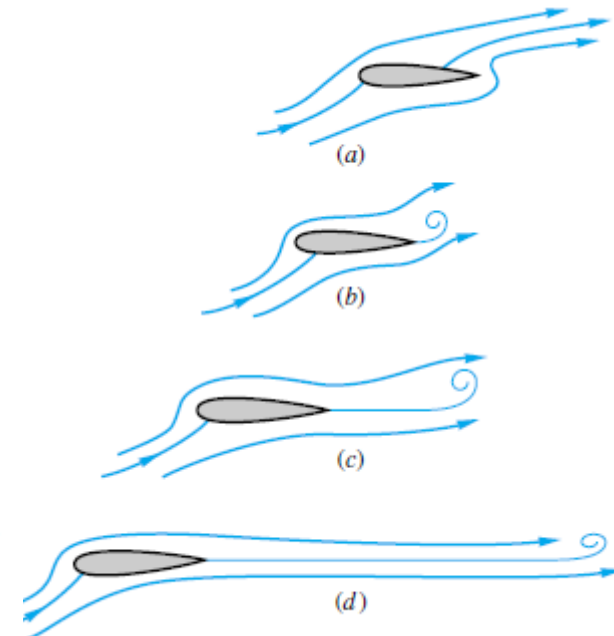Fig. 7.22 Definition sketch for a lifting vane.

Fig. 7.23 Transient stages in the development of lift: (*a*) start-up: rear stagnation point on the upper surface: no lift; (*b*) sharp trailing edge induces separation, and a starting vortex forms: slight lift; (*c*) starting vortex is shed, and streamlines flow smoothly from trailing edge: lift is now 80 percent developed; (*d*) starting vortex now shed far behind, trailing edge now very smooth: lift fully developed.

At a low angle of attack, the rear surfaces have an adverse pressure gradient but not enough to cause significant boundary-layer separation. The flow pattern is smooth, as in Fig. 7.23d, and drag is small and lift excellent. As the angle of attack is increased, the upper-surface adverse gradient becomes stronger, and generally a *separation bubble* begins to creep forward on the upper surface.[6] At a certain angle $\alpha = 15$ to $20°$, the flow is separated completely from the upper surface, as in Fig. 7.24. The airfoil is said to be *stalled*: Lift drops off markedly, drag increases markedly, and the foil is no longer flyable.

Figure 7.25 shows the lift and drag on a symmetric airfoil denoted as the NACA 0009 foil, the last digit indicating the thickness of 9 percent. With no flap extended, this airfoil, as expected, has zero lift at zero angle of attack. Up to about 12° the lift coefficient increases linearly with a slope of 0.1 per degree, or 6.0 per radian. This is in agreement with the theory outlined in Chap. 8:

$$C_{L,\text{theory}} \approx 2\pi \sin\left(\alpha + \frac{2h}{c}\right) \qquad (7.67)$$

where h/c is the maximum camber expressed as a fraction of the chord. The NACA 0009 has zero camber; hence $C_L = 2\pi \sin \alpha \approx 0.11\alpha$, where α is in degrees. This is excellent agreement.

Fig. 7.24 At high angle of attack, smoke-flow visualization shows stalled flow on the upper surface of a lifting vane. [*From Ref. 19, Illustrated Experiments in Fluid Mechanics* (*The NCFMF Book of Film Notes*), National Committee for Fluid Mechanics Films, Education Development Center, Inc., copyright 1972.]
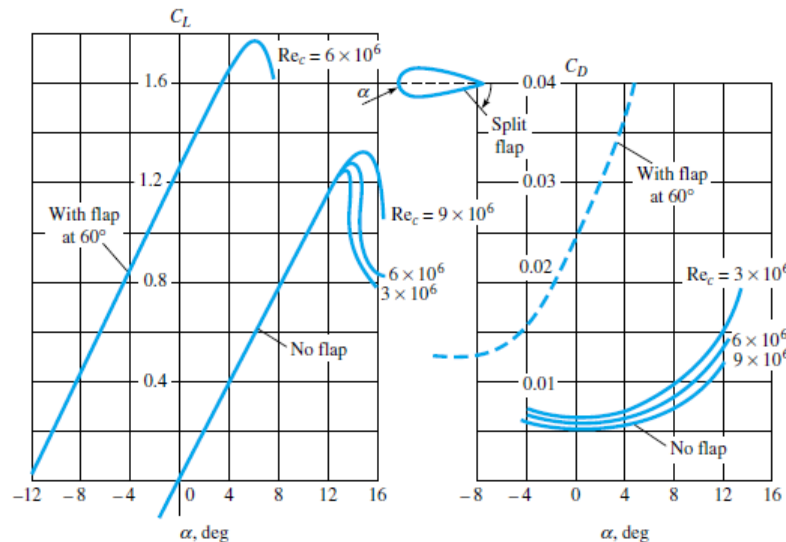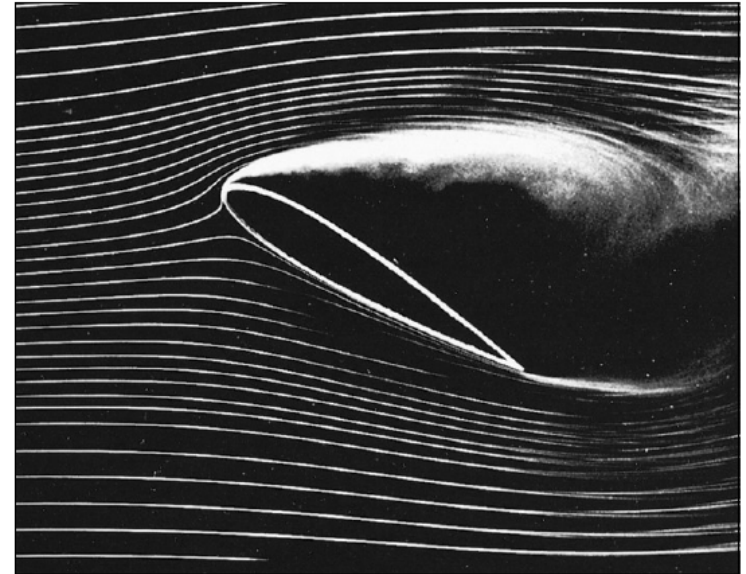

Fig. 7.25 Lift and drag of a symmetric NACA 0009 airfoil of infinite span, including effect of a split-flap deflection. Note that roughness can increase C_D from 100 to 300 percent.

Chapter 8

Review of Velocity-Potential Concepts

$$\mathbf{V} = \nabla\phi \qquad \text{or} \qquad u = \frac{\partial\phi}{\partial x} \qquad v = \frac{\partial\phi}{\partial y} \qquad w = \frac{\partial\phi}{\partial z} \tag{8.1}$$

The continuity equation (4.73), $\nabla \cdot \mathbf{V} = 0$, reduces to Laplace's equation for ϕ:

$$\nabla^2\phi = \frac{\partial^2\phi}{\partial x^2} + \frac{\partial^2\phi}{\partial y^2} + \frac{\partial^2\phi}{\partial z^2} = 0 \tag{8.2}$$

and the momentum equation (4.74) reduces to Bernoulli's equation:

$$\frac{\partial\phi}{\partial t} + \frac{p}{\rho} + \frac{1}{2}V^2 + gz = \text{const} \qquad \text{where } V = |\nabla\phi| \tag{8.3}$$

Typical boundary conditions are known free-stream conditions

Outer boundaries: $\qquad\qquad$ Known $\dfrac{\partial\phi}{\partial x}, \dfrac{\partial\phi}{\partial y}, \dfrac{\partial\phi}{\partial z}$ $\qquad\qquad$ (8.4)

and no velocity normal to the boundary at the body surface:

Solid surfaces: $\qquad \dfrac{\partial\phi}{\partial n} = 0 \qquad$ where n is perpendicular to body $\qquad$ (8.5)

Unlike the no-slip condition in viscous flow, here there is *no* condition on the tangential surface velocity $V_s = \partial\phi/\partial s$, where s is the coordinate along the surface. This velocity is determined as part of the solution to the problem.

Occasionally the problem involves a free surface, for which the boundary pressure is known and equal to p_a, usually a constant. The Bernoulli equation (8.3) then supplies a relation at the surface between V and the elevation z of the surface. For steady flow, e.g.,

Free surface: $\qquad\qquad V^2 = |\nabla\phi|^2 = \text{const} - 2gz_{\text{surf}} \qquad\qquad$ (8.6)
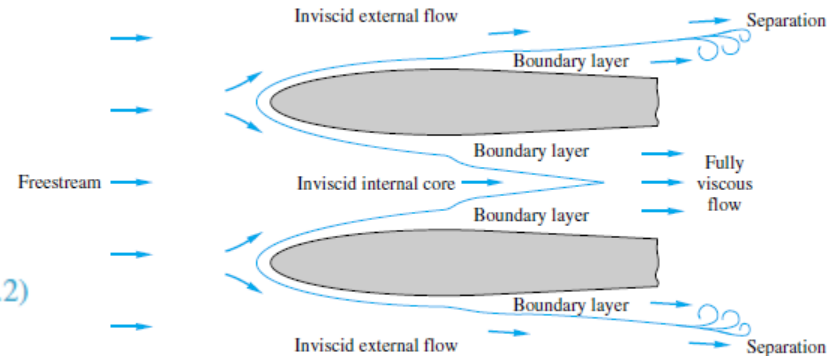

Fig. 8.1 Patching viscous- and inviscid-flow regions. Potential theory in this chapter does not apply to the boundary-layer regions

Chapter 8 (Cont'd)

Review of Stream Function
Concepts

Recall from Sec. 4.7 that if a flow is described by only two coordinates, the stream function ψ also exists as an alternate approach. For plane incompressible flow in xy coordinates, the correct form is

$$u = \frac{\partial \psi}{\partial y} \qquad v = -\frac{\partial \psi}{\partial x} \tag{8.7}$$

The condition of irrotationality reduces to Laplace's equation for ψ also:

$$2\omega_z = 0 = \frac{\partial v}{\partial x} - \frac{\partial u}{\partial y} = \frac{\partial}{\partial x}\left(-\frac{\partial \psi}{\partial x}\right) - \frac{\partial}{\partial y}\left(\frac{\partial \psi}{\partial y}\right)$$

or

$$\frac{\partial^2 \psi}{\partial x^2} + \frac{\partial^2 \psi}{\partial y^2} = 0 \tag{8.8}$$

The boundary conditions again are known velocity in the stream and no flow through any solid surface:

Free stream: $\qquad\qquad$ Known $\dfrac{\partial \psi}{\partial x}, \dfrac{\partial \psi}{\partial y}$ $\qquad\qquad$ (8.9a)

Solid surface: $\qquad\qquad$ $\psi_{\text{body}} = \text{const}$ $\qquad\qquad$ (8.9b)

Equation (8.9b) is particularly interesting because *any* line of constant ψ in a flow can therefore be interpreted as a body shape and may lead to interesting applications.

For the applications in this chapter, we may compute either ϕ or ψ or both, and the solution will be an *orthogonal flow net* as in Fig. 8.2. Once found, either set of lines may be considered the ϕ lines, and the other set will be the ψ lines. Both sets of lines are laplacian and could be useful.
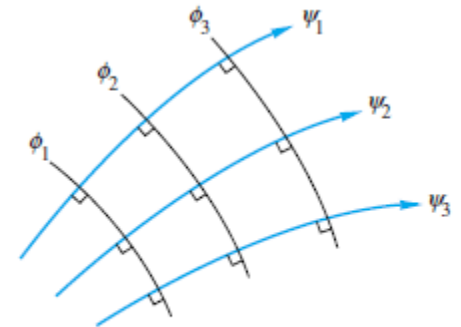
(a)
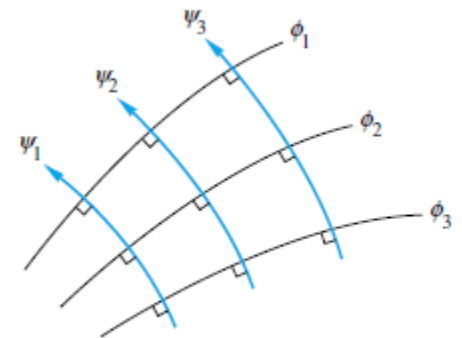
(b)

Fig. 8.2 Streamlines and potential lines are orthogonal and may reverse roles if results are useful: (a) typical inviscid-flow pattern; (b) same as (a) with roles reversed.

Plane Polar Coordinates

Many solutions in this chapter are conveniently expressed in polar coordinates (r, θ). Both the velocity components and the differential relations for ϕ and ψ are then changed, as follows:

$$v_r = \frac{\partial \phi}{\partial r} = \frac{1}{r}\frac{\partial \psi}{\partial \theta} \qquad v_\theta = \frac{1}{r}\frac{\partial \phi}{\partial \theta} = -\frac{\partial \psi}{\partial r} \qquad (8.10)$$

Laplace's equation takes the form

$$\frac{1}{r}\frac{\partial}{\partial r}\left(r\frac{\partial \phi}{\partial r}\right) + \frac{1}{r^2}\frac{\partial^2 \phi}{\partial \theta^2} = 0 \qquad (8.11)$$

Exactly the same equation holds for the polar-coordinate form of $\psi(r, \theta)$.

8.2 Elementary Plane-Flow Solutions

Uniform stream iU:	$\psi = Uy$	$\phi = Ux$	(8.12a)
Line source or sink:	$\psi = m\theta$	$\phi = m \ln r$	(8.12b)
Line vortex:	$\psi = -K \ln r$	$\phi = K\theta$	(8.12c)

The source "strength" m and the vortex "strength" K have the same dimensions, namely, velocity times length, or $\{L^2/T\}$.

If the uniform stream is written in plane polar coordinates, it becomes

Uniform stream iU:	$\psi = Ur \sin \theta$	$\phi = Ur \cos \theta$	(8.13)

This makes it easier to superimpose, say, a stream and a source or vortex by using the same coordinates. If the uniform stream is moving at angle α with respect to the x-axis,

$$\psi = U(y \cos \alpha - x \sin \alpha) \qquad \phi = U(x \cos \alpha + y \sin \alpha) \qquad (8.14)$$

Circulation

The line-vortex flow is irrotational everywhere except at the origin, where the vorticity $\nabla \times \mathbf{V}$ is infinite. This means that a certain line integral called the *fluid circulation* Γ does not vanish when taken around a vortex center.

With reference to Fig. 8.3, the circulation is defined as the counterclockwise line integral, around a closed curve C, of arc length ds times the velocity component tangent to the curve

$$\Gamma = \oint_C V \cos \alpha \, ds = \int_C \mathbf{V} \cdot d\mathbf{s} = \int_C (u \, dx + v \, dy + w \, dz) \qquad (8.15)$$

From the definition of ϕ, $\mathbf{V} \cdot d\mathbf{s} = \nabla\phi \cdot d\mathbf{s} = d\phi$ for an irrotational flow; hence normally Γ in an irrotational flow would equal the final value of ϕ minus the initial value of ϕ. Since we start and end at the same point, we compute $\Gamma = 0$, but not for vortex flow: With $\phi = K\theta$ from Eq. (8.12c) there is a change in ϕ of amount $2\pi K$ as we make one complete circle:

Path enclosing a vortex: $\qquad\qquad\qquad \Gamma = 2\pi K$

In general, Γ denotes the net algebraic strength of all the vortex filaments contained within the closed curve. In the next section we shall see that a region of finite circulation within a flowing stream will be subjected to a lift force proportional to both U_∞ and Γ.

It is easy to show, by using Eq. (8.15), that a source or sink creates no circulation. If there are no vortices present, the circulation will be zero for any path enclosing any number of sources and sinks.
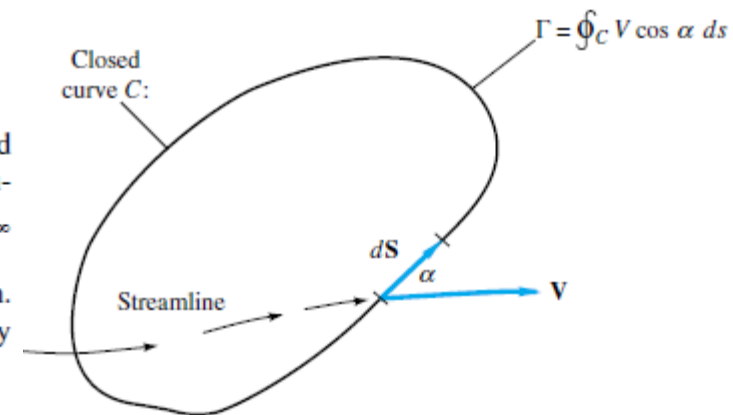

Fig. 8.3 Definition of the fluid circulation Γ.

8.3 Superposition of Plane-Flow Solutions

Rankine half-body:

$$\psi = U_\infty r \sin\theta + m\theta \qquad \phi = U_\infty r \cos\theta + m \ln r$$
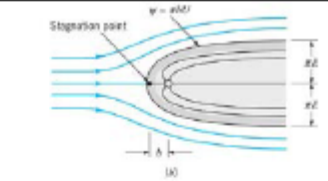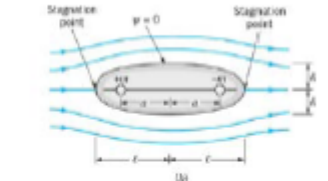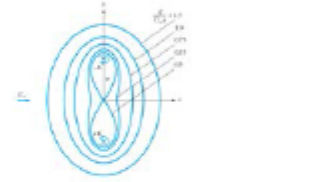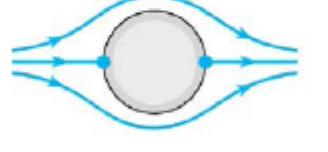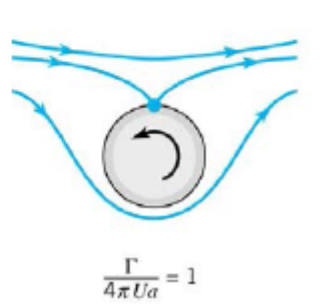
The Rankine Oval

$$\psi = U_\infty y - m \tan^{-1}\frac{2ay}{x^2 + y^2 - a^2} = U_\infty r \sin\theta + m(\theta_1 - \theta_2)$$

The Kelvin Oval

$$\psi = U_\infty y - \frac{1}{2} K \ln\frac{x^2 + (y + a)^2}{x^2 + (y - a)^2}$$

Flow Past a Circular Cylinder with Circulation

$$\psi = U_\infty \sin\theta\left(r - \frac{a^2}{r}\right) - K \ln\frac{r}{a}$$

Body name	Elemental combination	Flow Patterns
Rankine Half Body	Uniform stream+source	
Rankine Oval	Uniform stream+source+sink	
Kelvin Oval	Uniform stream+vortex point	
Circular Cylinder without circulation	Uniform stream+doublet	
Circular Cylinder with circulation	Uniform stream+doublet+vortex	$\frac{\Gamma}{4\pi U a} = 1$

Chapter 8 (Cont'd)

8.6 Images[3]

Spherical and Curvilinear Boundaries:

The results for plane boundaries are obtained from consideration of symmetry. For spherical and circular boundaries, image systems can be determined from the Sphere & Circle Theorems, respectively. For example:

| Flow field	Image System
Source of strength M at c outside sphere of radius a, c>a	Sources of strength ma/c at a^2/c and line sink of strength m/a extending from center of sphere to a^2/c
Dipole of strength μ at l outside sphere of radius a, l>a	dipole of strength $-a^3\mu/l$ at $-a^2/l$
Source of strength m at b outside circle of radius a, b>a	equal source at a^2/b and sink of same strength at the center of the circle

(a)

(b)
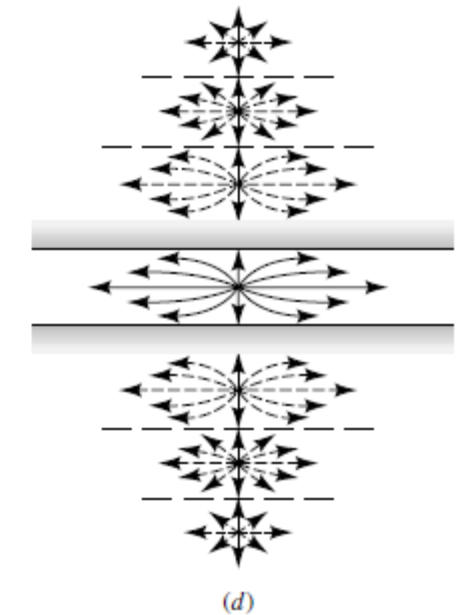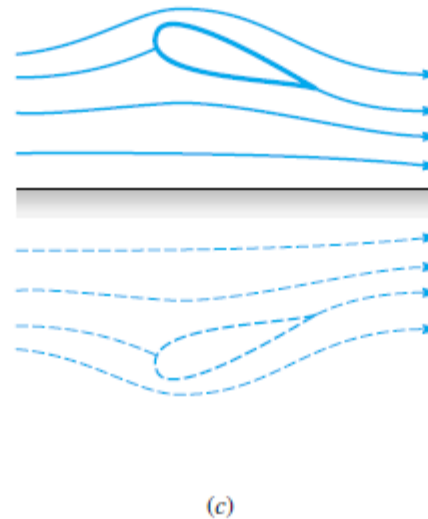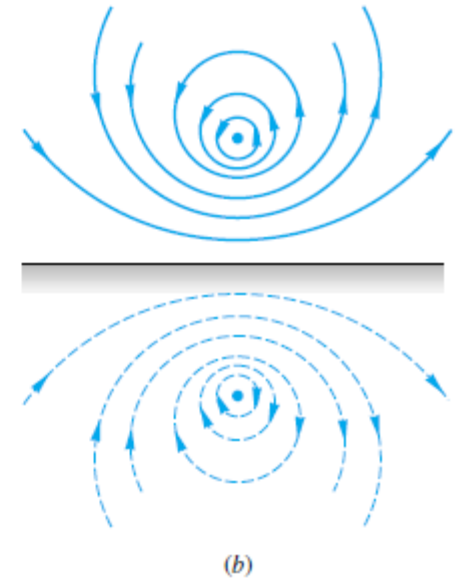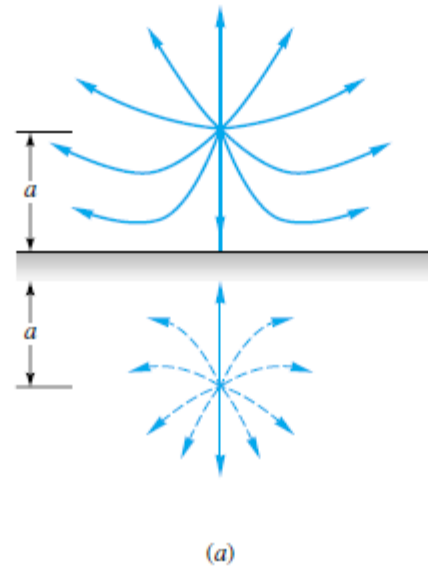
Fig. 8.17 Constraining walls can be created by image flows: (a) source near a wall with identical image source; (b) vortex near a wall with image vortex of opposite sense; (c) airfoil in ground effect with image airfoil of opposite circulation; (d) source between two walls requiring an infinite row of images.

(c)

(d)